Poly(dimethylsilylene)diacetylenes Guided ZIF-based Heterostructures for Full Ku-Band Electromagnetic Wave Absorption

Peng Miao,[†] Kaiyang Cheng,[§] Hongqiang Li,[§] Junwei Gu,[†] Kaijie Chen,[†] Steven Wang,[‡] Ding Wang,[〃] Terence X. Liu,[〃] Ben B. Xu*[〃] and Jie Kong*[†]

[†]MOE Key Laboratory of Materials Physics and Chemistry in Extraordinary Conditions, Shaanxi Key Laboratory of Macromolecular Science and Technology, School of Science, Northwestern Polytechnical University, Xi'an, 710072, P. R. China.

[§]MOE Key Laboratory of Advanced Micro-structure Materials, School of Physics Science and Engineering, Tongji University, Shanghai, 200092, P.R. China.

[‡]School of Chemical Engineering and Advanced Materials, Newcastle University, Newcastle University, Newcastle Upon Tyne, NE1 7RU, U.K.

[〃]Mechanical and Construction Engineering, Faculty of Engineering and Environment, Northumbria University, Newcastle upon Tyne, NE1 8ST, U.K.

Abstract

Zeolitic imidazolate frameworks (ZIFs), a group of metal–organic frameworks (MOFs), hold promise as building blocks in electromagnetic (EM) wave absorption/shielding materials and devices. In this contribution, we proposed a facile strategy to synthesize three dimensional ZIF-67-based hierarchical heterostructures through coordinated reacting a preceramic component, poly(dimethylsilylene)diacetylenes (PDSDA) with ZIF-67, following by carbonizing the PDSDA wrapped ZIF at high temperature. The introduction of PDSDA leads to a controllable generation of surface network containing branched carbon nanotubes and regional distributed graphitic carbons, in addition to the nanostructures with well-defined size and porous surface made by cobalt nanoparticles. The surface structures can be tailored through variations in pyrolysis temperatures, therefore enabling a simple and robust route to facilitate suitable structural surface. The heterostructure of ZIF nanocomplex allows the existence of dielectric loss and magnetic loss, therefore, yielding a significant improvement on EM wave absorption with a minimum reflection coefficient (RC_{min}) of -50.9 dB at 17.0 GHz at a thickness of 1.9 mm and an effective absorption bandwidth (EAB) covering the full Ku-band (12.0 GHz to 18.0 GHz).

Keywords: zeolitic imidazolate frameworks, electromagnetic wave absorbing, nanocomplex, heterostructure, coordination reaction

Introduction

Metal-organic frameworks (MOFs) have attracted significant interests in last decades from various fields such as absorbent materials for gas separation, energy storage, luminescence materials, bio-sensors.[1-5] The high designability on functionalities for MOFs can be facilitated via changing the precursors and/or synthetic conditions,[6,7] as well as post-synthesis modifications (extended annealing, etc.).[8-10] Recently, a sub-group of MOFs, zeolitic imidazolate framework (ZIF), has been seen as a rising material with high porosity,[11,12] excellent mechanical stability,[13] tunable surface properties[14,15] and their exceptional chemical and thermal stabilities.[11,16] ZIFs also offer excellent configurability on structures by substituting the metal centre with other ions,[5,17,18] such as Cu^{2+}, Ni^{2+}, Cd^{2+}, yielding zeolite-like structures,[19,20] which is desired for electromagnetic (EM) wave absorbing/shielding.[21-30] The ultra-wide band absorption in specific band such as Ku-band (12-18 GHz), X-band (8.2-12.4 GHz) for EM wave absorbing materials is always important for their application in wireless communication, satellite communication, medical and aerospace fields.[31,32]

Thus far, the ZIF faces challenges to achieve a high real permittivity (ε') and poor impedance matching after pyrolysis, which lead to a strong reflectivity of EM wave on surface and a poor performance on EM wave absorption. One potential solution is to construct structural surface with using low dielectric materials to ‘trap’ the EM wave on surface. The concept remains yet to achieve due to the challenges in facilitating nanostructures during multi-step synthesis and the withholding of synthesized structure during pyrolysis at high temperature during the post synthesis treatment. Ceramic materials with lower complex permittivity can essentially bridge the gap and provide good electromagnetic wave absorption properties.[33-35] Dedicated

heterostructure from ceramics can be achieved by introducing the polymeric ceramic precursors into the multi-stage synthesis, resulting into a controllable generation of surface structure after pyrolysis. However, this route has been less considered in ZIF-based nanomaterials.

Here, we proposed a facile strategy to synthesis ZIF-67-based nanocomplex with hierarchical structures by initializing a coordination reaction between poly(dimethylsilylene)diacetylenes (PDSDA), a polymeric ceramic precursor with lower complex permittivity with cobalt in ZIF-67.[36,37] After pyrolysis, we successfully prepared nanocomplex consisting of multi-lengthscale interfaces between core-shell structures with porous low dielectric external shell (formed by PDSDA), high permittivity magnetic core (formed by ZIF-67), carbon nanotubes (formed by amorphous carbon locally catalyzed by cobalt) on surface, and amorphous carbons. We demonstrate an enhanced EM wave absorption with a minimum reflection coefficient (RC_{min}) of -50.9 dB at 17.0 GHz with a sample thickness of 1.9 mm and an effective absorption bandwidth (EAB) covering the full Ku-band (12.0 GHz to 18.0 GHz) with designable heterostructure.

Experimental Section

Materials. The dichlorodimethylsilane (98%), trichloroethylene (>98%), hexachloro-1, 3-butadiene (97%), n-butyllithium (1.6 M solution in hexanes) and N, N-dimethylformamide (DMF) were purchased from Alfa Aesar China (Tianjin, China). The cobalt nitrate hexahydrate (99.99 % metals basis) was bought from Macklin Co. (Shanghai, China) and 2-methylimidazole (99%) was purchased from TCI Co. (Shanghai, China). All other reagents were used as received.

Synthesis of poly(dimethylsilylene)diacetylenes (PDSDA). The synthesis of **PDSDA** was conducted using a standard Schlenk technique.[38,39] The 0.14 mol (42.51 g) n-butyllithium was

dissolved in 60 mL THF at -78 °C in an acetone/dry ice bath under an argon atmosphere. Then 0.035 mol (9.456 g) hexachloro-1, 3-butadiene was added through an argon-purged syringe. Subsequently, 0.035 mol dichlorodimethylsilane (4.578 g) was dropped into the flask at −78 °C. After stirring at room temperature for 12 h, the chlorotrimethylsilane (2 mL) was added. Then the mixture was dissolved in toluene to filter out the lithium chloride The polymer was precipitated in methanol and dried under vacuum environment. Finally the alkyne-containing PDSDA was obtained.

Syntheses of ZIF-67 and pre-pyrolyzed **ZIF-67.** The ZIF-67 was synthesized according to references.[40-42] 1.5 mmol of cobalt nitrate in 12 mL deionized water and 67 mmol of dimethylimidazole in 80 mL deionized water were mixed and stirred vigorously for 6 h. After stirring 24 h, the purple precipitates were collected by centrifugation three times using methanol as eluent. Finally, the as-prepared ZIF-67 was purple solid. The ZIF-67 was pyrolyzed at 500°C for 2 h (heating rate 5 K/min under argon) in tube finance to prepare pre-pyrolyzed ZIF-67 (P-ZIF-67). The 0.02g of PDSDA and 0.1g of pre-pyrolyzed ZIF-67 were mixed in DMF at room temperature under ultrasonic for 4 h, to fulfill the coordinated reaction to get P-ZIF-67 wrapped with PDSDA.

Preparation of ZIF-67-based nanocomplex. The P-ZIF-67 wrapped with PDSDA was pyrolyzed at various temperatures (500 °C, 600 °C, 700 °C and 800 °C) under an argon atmosphere in the tube furnace (GSL-1700X, Kejing New Mater. Ltd., Hefei, China). The obtained Co/Si/C/N nanocomplex was named as Co/Si/C/N-500, Co/Si/C/N-600, Co/Si/C/N-700 and Co/Si/C/N-800, respectively, according to the pyrolyzed temperature.

Characterization. Fourier transform infrared spectroscopy (FT-IR) measurement was performed on a FT-IR spectrometer (DSOR 27, Bruck, Germany). Thermogravimetric analysis and mass spectrometry analysis were conducted on a simultaneous thermal device (STA, 449C Jupiter, Netzsch, Gerätebau GmbH, Selb, Germany) coupled with a quadrupole mass spectrometer. The flow of argon is 40 mL/min and the heating rate is 10 K/min, respectively. The crystal structure was analyzed by using X-ray diffractometer (XRD) (Rigaku D/Max-2550VB+/PC) with Cu Kα irradiation (λ =1.54178 Å, 40.0 kV, 40.0 mA). The scanning electron microscopy (SEM) (Hitachi-S-4800) and the transmission electron microscopy (TEM) (FEI Talos-F200X) were used to observe the morphology and elemental distribution of samples. The Raman spectrum (Invia, Renishaw, USA) was equipped with 514 nm Ar laser excitation device. The Micrometrics Tristar 3020 (Micromeritics Co.) nitrogen adsorption instrument was used to measure specific surface and pore size distribution (Brunauer-Emmett-Teller, BJH model). The magnetic hysteresis loop was measured using a vibrating sample magnetometer (Lake Shore VSM 7307) at 298.15 K.

EM wave absorbing measurement. The complex permittivity and complex permeability of Co/Si/C/N heterostructure nanocomplex were measured using a vector network analyzer (VNA, MS4644A, Anritsu) in the frequency range of 2−18 GHz. The milled Co/Si/C/N samples were dispersed in paraffin matrix with 30 % mass fraction to form the coaxial rings with an inner diameter of 3.04 mm and an outer diameter of 7.0 mm. On the basis of the generalized transmission line theory and metal backplane model,[43,44] the reflection coefficient (RC) can be calculated using relative complex permittivity according to the following equation.[45]

$$RC = 20\log_{10}\left|\frac{Z_{in}-1}{Z_{in}+1}\right| \qquad (1)$$

$$Z_{in} = \sqrt{\frac{\mu_r}{\varepsilon_r}} \tanh\left[j \frac{2\pi fd}{c} \sqrt{\mu_r \varepsilon_r} \right] \qquad (2)$$

where Z_{in}, ε_r and μ_r is the normalized input impedance, permittivity, and permeability of the materials, respectively. The *f, d* and c represents the frequency, thickness (m) and the velocity of the EM wave in vacuum, respectively.

Results and Discussion

The synthesis route of ZIF-67-based heterostructure nanocomplex is schematically illustrated in **Figure 1a**, where the ZIF-67 is prepared from cobalt nitrate and 2-methylimidazole (Step I).[40,41,43] The pre-pyrolyzed ZIF-67 (Step II) represents a basic polyhedral geometry with 80 % yield as shown in Supporting Information (**Figure S1**) with a number of cobalt atoms. In Step III and Step IV, the PDSDA was wrapped on ZIFs to fulfill low complex permittivity and high ceramic yield (**Figure S1**) in the final nanocomplex. The complete disappearance of alkenyl peak at 2100 cm^{-1} in FT-IR (**Figure S2**) suggests that coordination reaction successfully occurs between the transitional metal ions (Co^{2+}) with the alkenyl groups in PDSDA.[39] After pyrolysis at high temperatures (500 °C or above) under Ar atmosphere (Step V), we successfully obtain the ZIF-67-based heterostructure nanocomplex (**Figure1b**), which are assumed to have core-shell structure (**Figure 1a**) with low dielectric shell (formed by PDSDA) and high real permittivity (ε'), magnetic core (formed by ZIF-67) and branched carbon nanotubes on surface as metal Co could indorse graphitic carbon to form carbon nanotubes and amorphous carbons.[46-48] The samples are labeled as Co/Si/C/N-500, Co/Si/C/N-600, Co/Si/C/N-700, Co/Si/C/N-800, respectively, where the digital number refers to the pyrolysis temperature.

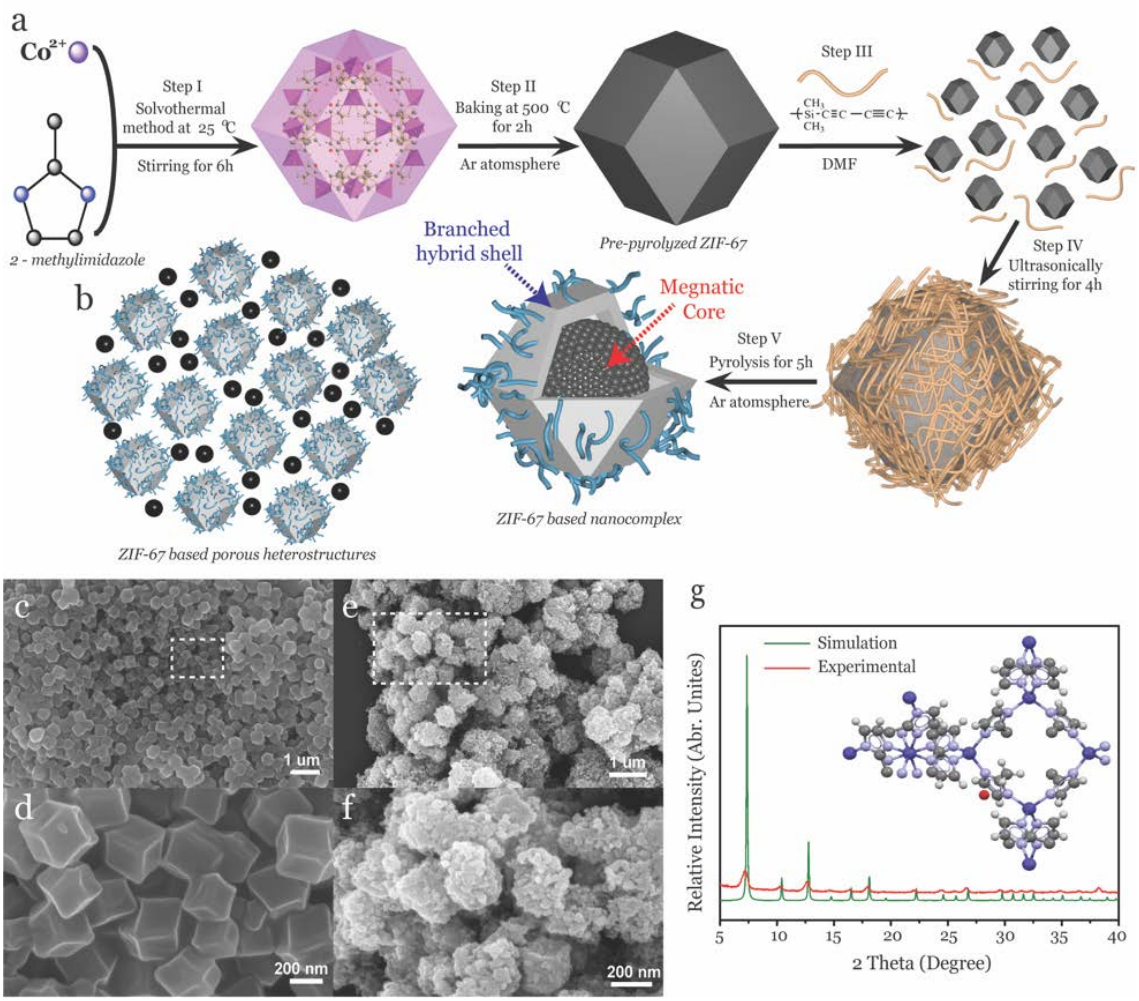

Figure 1 Schematic illustration of the fabrication route towards ZIF-67-based heterostructure nanocomplex (a, b), SEM images of ZIF-67 (c) after Step II in (a) with the magnified observation (d) in the selected area, the morphology of ZIF-67-based heterostructure nanocomplex with the magnified observation in the selected area (e, f), theoretical and experimental XRD results for ZIF-67 crystal (g).

The morphology and structure of pre-pyrolyzed ZIF-67 and their derived nanocomplex were evaluated by scanning electron microscopy (SEM, **Figure 1c-f**), where we observed typical rhombic dodecahedron morphology for pre-pyrolyzed ZIF-67 (**Figure 1c-d**) in a size distribution of 300 - 400 nm.[49,50] After initializing the coordinated reaction with PDSDA on ZIF surface and pyrolyzing at high temperature, we obtain a highly mesoporous surface on ZIF-based

nanocomplex (**Figure 1e-f**). The powder X-ray diffraction (XRD) result for pre-pyrolyzed ZIF-67 (**Figure 1g**) suggests a sodalite topology of ($Co(mIM)_2$) in good agreement to the theoretical crystal structure. Overall, the good preservation in dodecahedron shape was presented after pyrolyzing at high temperatures.[51,52]

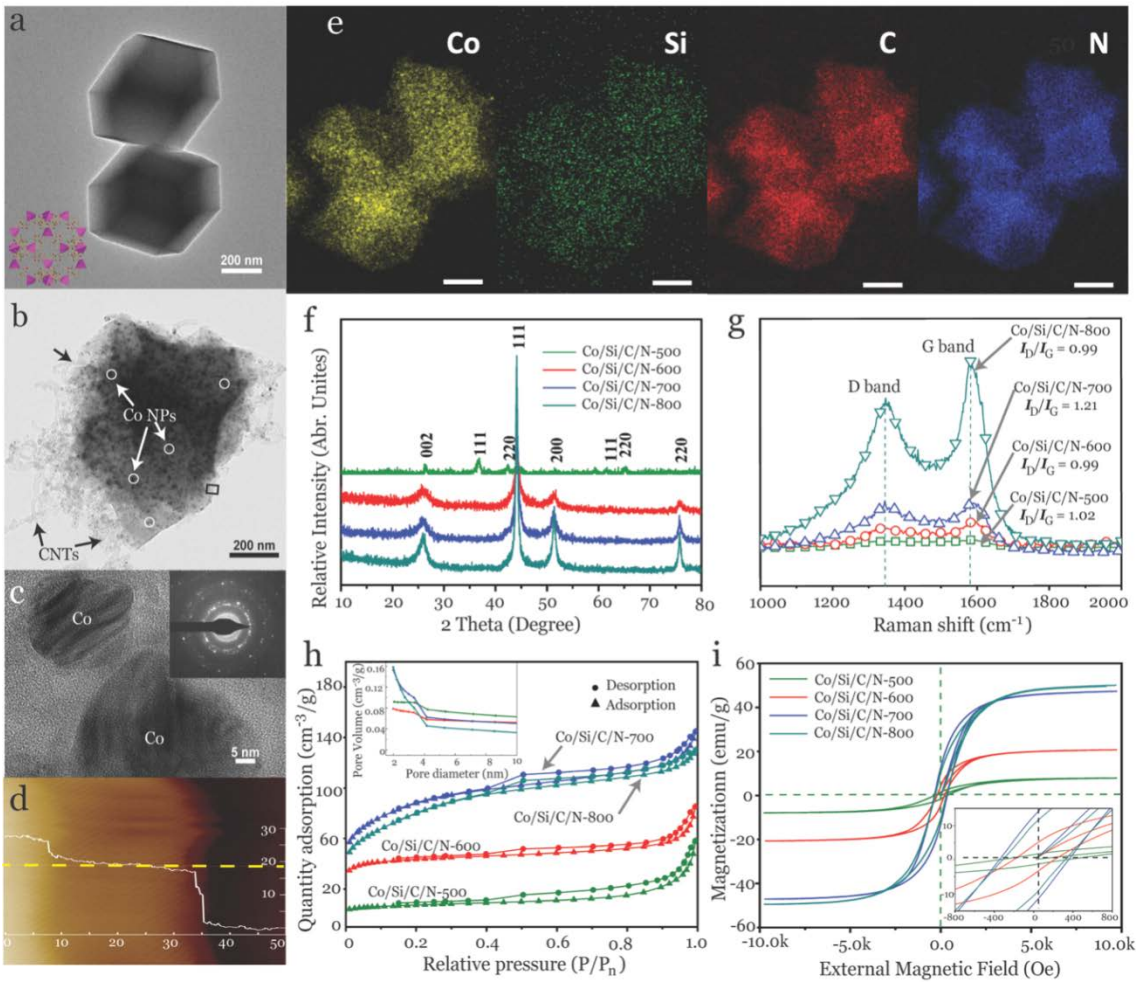

Figure 2 The TEM images of pre-pyrolyzed ZIF-67 crystals collected after Step II (a), ZIF-67-based heterostructure nanocomplex after Step V (b), with the magnified observation on Co nanoparticles and SAED image (inset) in (c)., the AFM profile (d) of the selected area in (b), the EDS mapping (Co, Si, C, N) (e) for the nanocomplex in (b), XRD (f) and Raman results (g) for the nanocomplex under different temperature, N_2 adsorption and pore size distribution plots (h) and hysteresis loop and coercivity (inset) of nanocomplex (i).

By thermally pyrolyzing at an inert atmosphere, the organic ligands in ZIF-67 crystal (**Figure 2a**) can be carbonized and metal ions will be reduced to form a hybrid metal/carbon structure.[53,54] By characterizing the pyrolyzed ZIF-based nanocomplex using TEM, we found (i) clear boundaries as being defined by original ZIF (**Figure 2b**) covered by (ii) highly branched carbon nanotubes (CNTs, typically ca. 10 nm in diameter and ca. a few micrometers in length), (iii) a mesoporous surface where metallic cobalt particles (**Figure 2c**) were formed. After the decomposition and carbonization, most of the cobalt deposit outside of the carbon matrix to form a porous shell. The corresponding selected area electron diffraction (SAED) pattern (inset, **Figure 2c**) confirms that polycrystallinity phase occur for the pyrolyzed ZIF-67. The organic ligands in PDSDA were catalyzed by cobalt to generate CNTs on the surface, as well as graphene skirts regionally located at the edge of nanocomplex (**Figure 2d**).

From the EDS mapping in **Figure 2e**, we find a uniform distribution of C (red), Si (green) and N (blue) with the same profile of pre-pyrolyzed ZIF (labelled by Co), which prove the homogeneity coverage of the branched CNTs on the ZIF nanocomplex. We next assess the elemental and valance states for ZIF-67 based nanocomplex at 700 °C using XPS (**Figure S3a**). The high-resolution C 1s spectrum (from 282 eV to 292 eV, **Figure S3b**) reveals four types of carbon bonds corresponding to C-C (284.6 eV), C-N (285.4 eV), C-O (286.5 eV), O-C=O (289.2 eV).[39,55-57] The Co 2p spectrum (from 773 eV to 789 eV for Co 2p 3/2 and from 790 eV to 809 eV for Co 2p 1/2, **Figure S3c**) agrees well to four signature peaks, i.e. Co (779.0 eV), Co trivalent (783.6 eV) and bivalent (794.5 eV and 800 eV). The divalent cobalt is oxidized to trivalent cobalt when being exposed in the air.[58] The N 1s spectrum (from 395 eV to 405 eV, **Figure S3d**) deconvolute into pyridinium-N at 398.5 eV, pyrrole nitrogen at 400.3 eV, graphitic

nitrogen at 401.3 eV, and nitric oxide at 404.5 eV.[59] The Si 2p spectrum from (98 eV to 106 eV, **Figure S3e**) indicates the coexistence of three deconvoluted peaks of SiC (100.8 eV), SiO_xC_y (102.5 eV) and SiO_2 (103.4 eV).[60] Combined with the TGA curve (green) in **Figure S1**, the PDSDA seems only partially degraded under 700 °C and 800 °C, indicating a transition layer can be formed.

We next investigated the temperature dependent phase composition and morphology changes for the synthesized nanocomplex by analyzing the powder XRD results (**Figure 2f**). Weak diffraction peaks are found for the Co/Si/C/N-500 at CoN (111), (220) crystal face at 2θ=36.9°, 2θ=61.7° (JCPDS#83-0831) and Co_2N (111), (200) crystal face at 2θ=42.5°, 2θ=65.3° (JCPDS#72-1368), respectively. However, no obvious characteristic peaks for CoN are shown for Co/Si/C/N-600, Co/Si/C/N-700 and Co/Si/C/N-800, indicating the collapse of CoN structure at 600°C. The diffraction peaks at 2θ=44.5°, 2θ=51.5°, 2θ=76.0° are assigned to (111), (200) and (220) crystal face of cubic Co crystals. The enhanced peak for graphitic carbons is observed when the pyrolysis temperature increases. The grain sizes for graphitic carbons and cubic Co are calculated using Debye-Scherrer equation.[50,61]

$$D = \frac{K\lambda}{\beta \cos\theta} \qquad (3)$$

where K=0.90, λ=0.154 nm, θ is diffraction angle and β is full width at half maxima of the most intense peak (FWHM). The calculated grain sizes for cubic cobalt atoms in Co/Si/C/N-600, Co/Si/C/N-700 and Co/Si/C/N-800 are 15.3 nm, 16.4 nm and 20.7 nm, respectively, the dendritic structure gradually grows on the surface of ZIF-67-based nanocomplex when the temperature increases to 600 °C and above (**Figure S4**).

Raman spectra are used to understand the morphological distribution of carbons in the pyrolyzed nanocomplex (**Figure 2g**). With the increase of pyrolysis temperature, the I_D/I_G of integrated intensity changes to represent the degree of disorder. Compared to Co/Si/C/N-600/800, the I_D/I_G of Co/Si/C/N-700 is higher, indicating a higher lattice disorder in sp^2-hybridized carbon atoms and/or deposition of amorphous carbon. The black spot (cobalt nanoparticles, **Figure 2b**) distributed around the dendritic polyhedron and causes hysteresis. Meanwhile, the branching dendrite extends free space and offer more contact surface, thus improve the impedance matching. The results of XRD in **Figure 2f** indicate clear polycrystalline phases, e.g. (111), (200), (220), for the metallic cobalt, which agrees well with TEM and SAED results as shown in **Figure 2c**.

We then analyzed the porosity of nanocomplex by plotting N_2 adsorption desorption curves using BJH calculation method (**Figure 2h**). All samples present typical type IV adsorption hysteresis characteristic loop at the nominal pressure (p/p_0) of 0.15-1.0 and 0.40-1.0.[62,63] The rapid increase of N_2 adsorption curve near the nominal pressure of 0.95 is attributed to the capillary condensation, revealing the presences of large pores in sample with a size distribution from 1.5 nm to 4.0 nm (see **Table S2**). For the ZIF67 crystals, the specific surface area is up to 2055.4 m^2/g. Due to the introduction of poly(dimethylsilylene)diacetylenes with high ceramic yield on surfaces, the specific surface area and pore size for the ZIF-based nanocomplex rapidly decreased when pyrolysis temperature increases. The small specific surface area for Co/Si/C/N-500 indicates an incomplete formation of porous structure at low temperature. The Co/Si/C/N-700 shows a high specific surface area of 319.2 m^2/g, whilst we discover a decrease on the

porosity for Co/Si/C/N -800, likely to occur once the skeleton structures collapse and/or partially damage at high temperature.

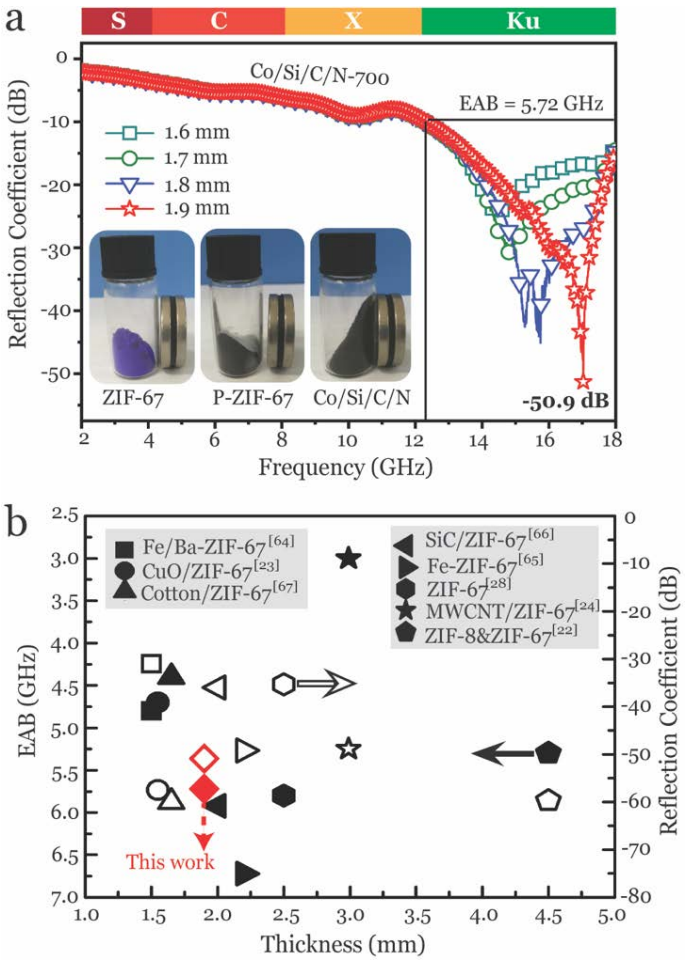

Figure 3 Reflection coefficient of Co/Si/C/N -700 at various thicknesses and demonstration of coercivity for ZIF-67, P-ZIF-67 and Co/Si/C/N -700 under magnetic field (a), comparison of the EM wave absorption properties for the ZIF-67-based nanocomplex with other reported values (b), where the solid symbol and hollow symbol refers to EAB and RC_{min}, respectively.

For electromagnetic wave absorption application, the general guideline suggests that more than 90 % of the incident EM wave will be absorbed when the value of reflection coefficient (RC) reaches -10 dB or less, which is considered as a key criterion to determine effective absorption bandwidth (EAB). By plotting the RC data for Co/Si/C/N porous complex at a frequency range

of 2-18 GHz (**Figure 3a**), RC_{min} value of -50.9 dB is found for Co/Si/C/N-700 with an EAB of 5.72 GHz, which covers almost the whole Ku-band (12-18 GHz). This excellent EM wave absorption property is enabled by the multi-length scale heterostructure formed after introducing PDSDA into ZIF-67, where the pyrolyzed material without PDSDA presents an opposite performance (**Figure S5**). It should also be noted that the complex presents a strong magnetic effect after pyrolysis (inset, **Figure 3a**), as part of unique feature for ZIF-67. The thickness dependent peak shift can be given by the following equation,[63]

$$t_m = \frac{\lambda}{4\sqrt{|\varepsilon_r \mu_r|}} = \frac{c}{4 f_m \sqrt{\varepsilon_r \mu_r}} \qquad (4)$$

where t_m and f_m is the thickness and frequency of peak dip, the λ and c represents the wavelength of the EM wave and the light velocity in vacuum, respectively. The Co/Si/C/N-700 presents the best EAB and RC_{min} performances among the rest samples (**Figure S6**), indicating that the optimized heterostructure is achieved at 700 °C. The ZIF-67 based complex in this research also presents advantage when comparing to the other reports (**Figure 3b**).

For transition metal/ZIF-67 complex systems, i.e. Zn/ZIF-67,[22] CuO/ZIF-67,[23] and Fe/Ba-ZIF-67,[64] the Co/Si/C/N-700 with a RC_{min} value of -50.9 dB and an EAB of 5.72 GHz shows the best EAB and RC_{min}. Even though Fe/ZIF-67 shows an EAB of 6.72 GHz and a RC_{min} of -49.2 dB when the mass fraction in paraffin matrix is as high as 40%,[65] the thickness and density are also much higher than the Co/Si/C/N nanocomplex. When it comes to silicon or carbon/ZIF-67 systems, e.g. MWCNT/ZIF-67,[24] SiC/ZIF-67,[66] cotton/Ba-ZIF-67,[67] our Co/Si/C/N nanocomplex also possess superior absorption in the whole Ku-band (12.0-18.0 GHz), where have not been reported elsewhere in silicon or carbon/ZIF-67 systems.

The EM wave absorbing performance is determined by complex permittivity and permeability. The real part (ε') of permittivity and the imaginary part (ε'') is related with polarization and dielectric loss ability, respectively. From the viewpoint of impedance matching, the low ε', high ε'' are favorable to the enhanced EM wave absorption, i.e. low reflection coefficient. As shown in **Figure S7**, the Z value of Co/Si/C/N-700 with a thickness of 1.9 mm is in the range of 0.8~1.0 in Ku-band, implying good impedance matching performance and excellent EM wave absorption. The attenuation constant α of Co/Si/C/N nanocomplex calculated through **Equ. 5** can access the dissipation effect for EM wave. The strong attenuation capability gradually increased in high frequency range as shown in **Figure S7**. Meanwhile, the best impedance matching as well as large attenuation ability of Co/Si/C/N-700 endows strong broadband absorbing performance.[52]

$$\alpha=\frac{\sqrt{2}\pi \mathrm{f}}{c}\times\sqrt{(\mu''\varepsilon''-\mu'\varepsilon')+\sqrt{(\mu'\varepsilon''+\mu''\varepsilon')^2+(\mu''\varepsilon''-\mu'\eta')^2}} \qquad (5)$$

Furthermore, in **Figure 4a**, the values of real part (ε') and imaginary part (ε") in 2-18 GHz for all samples are presented. For Co/Si/C/N-700, the ε' value is in the range of 10-42 in 2-10 GHz. With the frequency increases, the ε' gradually decreased to about 5. At the same time, the ε" (from 0.8 to 47) of Co/Si/C/N-700 is lower than that of other samples. Thus Co/Si/C/N-700 shows the low reflection coefficient and wide effective absorption bandwidth in Ku-band. The magnetic permeability of Co/Si/C/N nanocomplex is also sensitive to the frequency. As shown in **Figure 4b**, the real part (μ') and imaginary part (μ") increased in 2-18 GHz for Co/Si/C/N-500, Co/Si/C/N-600 and Co/Si/C/N-800, while the μ' decreased after 10 GHz for Co/Si/C/N-700. The μ" of Co/Si/C/N-700 is higher than that of Co/Si/C/N-500 and Co/Si/C/N-800 in 10-18 GHz. Overall, from the contribution of both dielectric loss and magnetic loss, the Co/Si/C/N-700 shows excellent EM absorption among all the nanocomplexes.

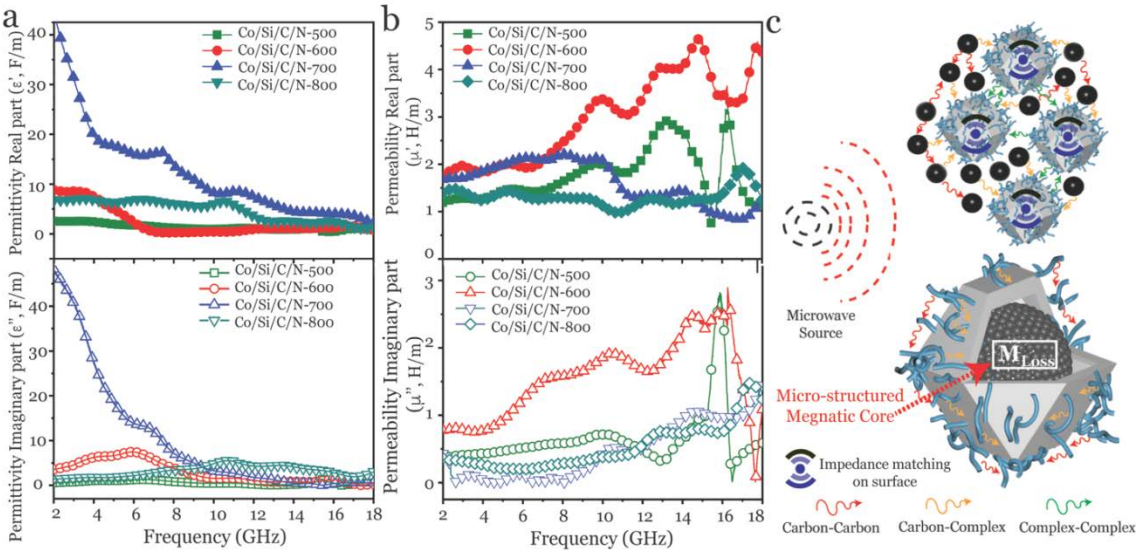

Figure 4 Complex permittivity plots (a) and permeability plots (b) for Co/Si/C/N nanocomplex, the illustration of hypothesized interfacial-driven electromagnetic wave attenuation for Co/Si/C/N nanocomplex (c).

As well known, the attenuation of EM wave is the consequence caused by the combined effects from dielectric loss and magnetic loss. Dielectric tangent loss ($tan\,\delta_\varepsilon = \varepsilon'' / \varepsilon'$) and magnetic tangent loss ($tan\,\delta_\mu = \mu'' / \mu'$) are calculated to assess the electromagnetic dissipation factors. **Figure S8** shows the value of electromagnetic loss with the Co/Si/C/N nanocomplex. It is obvious that the $\tan\delta_\varepsilon$ value of Co/Si/C/N-700 decreases as the frequency increases, whereas the $\tan\delta_\mu$ value shows an opposite trend. To well understand the effect of magnetic loss on the electromagnetic wave attenuation, we plot the hysteresis loop of the Co/Si/C/N porous complex in **Figure 2i**. The ZIF-67 and P-ZIF-67 only show linear paramagnetic response. However, the Co/Si/C/N nanocomplex shows strong ferromagnetic response with a gradually rising saturation magnetization (M_s) (7.9 emu/g, 20.6 emu/g, 47.3 emu/g, and 50.1 emu/g) when the pyrolysis temperature increases. Because the absolute values of susceptibility less than 1 ($|\chi|<1$, **Table**

S2), so the paramagnetic response of Co/Si/C/N nanocomplex can be judged. The magnetization is attributed to the CoN and Co_2N nanocrystals in nanocomplex. Since the Co/Si/C/N-700 possesses the highest remanence (M_r) of 13.2 emu/g and coercivity (H_c) of 350 Oe in comparison to other three samples (44-277 Oe), it can dissipate the EM wave into heat to attenuate at high frequency.[68]

Based on the analyses mentioned above, the illustration of hypothesized interfacial-driven electromagnetic wave attenuation for Co/Si/C/N nanocomplex is presented in **Figure 4c**. The heterostructured Co/Si/C/N nanocomplex consisting of low dielectric layer, porous structure and regular distribution of magnetic cobalt particles provides multiple interfaces to enable unique impedance matching and electromagnetic loss. The low dielectric layer like dendrite and porous structure can allow EM wave to enter the polyhedron and convert into heat and atomic vibration. The conductive network formed by amorphous carbon and cobalt particle can maximize the interfacial polarization loss. Ferromagnetism of the cobalt particle and transmission of low dielectric layer to high dielectric core allow more EM wave absorption rather than reflection, thus enhance the formation of magnetic eddy current.[69,70] The combining effect from multi-lengthscale structures among the interfaces contribute to outstanding EM wave absorption property together.

Conclusions

A facile strategy was developed to achieve ZIF-67-based heterostructured nanocomplex by introducing surface coordinated reaction between PDSDA and ZIF-67. The involvement of PDSDA allows the ZIF host to undergo significant surface morphological transformations by

carbonatizing the organic ligand during the pyrolysis. The nanocomplex possesses hierarchical heterostructure consisting of MOF framework defined by the original ZIF particles, nano-structured surface made by branched CNTs and regional distributed graphene skirt and a mesoporous surface based on Co particles. After further exploring the structure-functionality relationship for the nanocomplex, it demonstrates a unique EM wave absorption for the synthesized nanocomplex, by achieving a RC_{min} value of -50.9 dB and a EAB of 5.72 GHz at a thin thickness of 1.9 mm that almost covers the whole Ku-band (12.0-18.0 GHz). We expect this study of structural design of ZIF-based nanocomplex will open up a new window for developing high performance EM wave absorbing materials in future.

Associated Content

Author Information

*Corresponding Authors, E-mail Address: kongjie@nwpu.edu.cn (J.K.),

ben.xu@northumbria.ac.uk (B.X.).

Conflicts of Interest

There are no conflicts to declare.

Acknowledgements

This work was financially supported by the National Natural Science Foundation of China (21875190), the Natural Science Basic Research Plan in Shaanxi Province of China (2018JC-008, Distinguished Young Scholar), the Shaanxi Province Key Research and Development Plan

for Industry Innovation Chain (Cluster) (2018ZDCXL-GY-09-07), the Analytical and Testing Center of NPU and the Engineering and Physical Sciences Research Council (EPSRC) grants-EP/N007921 and EP/N032861/1.

Supporting Information

TGA-mass curves of polymers, XPS spectra and reflection coefficient of ceramics. The material is available free of charge via the Internet at http://pubs.acs.org.

References

(1) Han, L.; Yu, X. Y.; Lou, X. W. Formation of Prussian-Blue-Analog Nanocages via a Direct Etching Method and their Conversion into Ni-Co-Mixed Oxide for Enhanced Oxygen Evolution. *Adv. Mater.* **2016**, *28*, 4601-4605.

(2) Li, J. R.; Kuppler, R. J.; Zhou, H. C. Selective Gas Adsorption and Separation in Metal-Organic Frameworks. *Chem. Soc. Rev.* **2009**, *38*, 1477-1504.

(3) Zhang, W.; Lu, G.; Cui, C.; Liu, Y.; Li, S.; Yan, W.; Xing, C.; Chi, Y. R.; Yang, Y.; Huo, F. A Family of Metal-Organic Frameworks Exhibiting Size-Selective Catalysis with Encapsulated Noble-Metal Nanoparticles. *Adv. Mater.* **2014**, *26*, 4056-4060.

(4) Wu, H. B.; Lou, X. W. Metal-Organic Frameworks and Their Derived Materials for Electrochemical Energy Storage and Conversion: Promises and Challenges. *Sci. Adv.* **2017**, *3*, eaap9252.

(5) Saha, S.; Das, G.; Thote, J.; Banerjee, R. Photocatalytic Metal-Organic Framework from CdS Quantum Dot Incubated Luminescent Metallohydrogel. *J. Am. Chem. Soc.* **2014**, *136*, 14845-14851.

(6) Yoon, S. M.; Park, J. H.; Grzybowski, B. A. Large-Area, Freestanding MOF Films of Planar, Curvilinear, or Micropatterned Topographies. *Angew. Chem. Int. Ed.* **2017**, *56*, 127-132.

(7) Zhang, Z.; Chen, Y.; Xu, X.; Zhang, J.; Xiang, G.; He, W.; Wang, X. Well-defined Metal-Organic Framework Hollow Nanocages. *Angew. Chem. Int. Ed.* **2014**, *53*, 429-433.

(8) Zhuang, X.; Gehrig, D.; Forler, N.; Liang, H.; Wagner, M.; Hansen, M. R.; Laquai, F.; Zhang, F.; Feng, X. Conjugated Microporous Polymers with Dimensionality-controlled Heterostructures for Green Energy Devices. *Adv. Mater.* **2015**, *27*, 3789-3796.

(9) Kim, M.; Cahill, J. F.; Fei, H.; Prather, K. A.; Cohen, S. M. Postsynthetic Ligand and Cation Exchange in Robust Metal–Organic Frameworks. *J. Am. Chem. Soc.* **2012**, *134*, 18082-18088.

(10) Kaneti, Y. V.; Dutta, S.; Hossain, M. S. A.; Shiddiky, M. J. A.; Tung, K. L.; Shieh, F. K.; Tsung, C. K.; Wu, K. C.; Yamauchi, Y.Strategies for Improving the Functionality of Zeolitic Imidazolate Frameworks: Tailoring Nanoarchitectures for Functional Applications. *Adv. Mater.* **2017**, *29*, 1700213-1700244.

(11) Phan, A.; Doonan, C. J.; Uribe-Romo, F. J.; Knobler, C. B.; O'Keeffe, M.; Yaghi, O. M. Synthesis, Structure, and Carbon Dioxide Capture Properties of Zeolitic Imidazolate Frameworks. *Acc.Chem. Res.* **2010**, *43*, 58-67.

(12) Banerjee, R.; Phan, A.; Wang, B.; Knobler, C.; Furukawa, H.; O'Keeffe, M.; Yaghi, O. M. High-throughput Synthesis of Zeolitic Imidazolate Frameworks and Application to CO_2Capture. *Science* **2008**, *319*, 939-943.

(13) Tan, J. C.; Bennett, T. D.; Cheetham, A. K. Chemical structure, network topology, and porosity effects on the mechanical properties of Zeolitic Imidazolate Frameworks. *Proc. Natl. Acad. Sci. USA* **2010**, *107*, 9938-9943.

(14) Aromí, G.; Barrios, L. A.; Roubeau, O.; Gamez, P., Triazoles and tetrazoles: Prime ligands to generate remarkable coordination materials. *Coordin. Chem. Rev.* **2011**, *255* (5), 485-546.

(15) Morris, W.; Doonan, C. J.; Furukawa, H.; Banerjee, R.; Yaghi, O. M. Crystals as Molecules: Postsynthesis Covalent Functionalization of Zeolitic Imidazolate Frameworks. *J. Am. Chem. Soc.***2008**,*130*, 12626-12627.

(16) Wang, B.; Côté, A. P.; Furukawa, H.; O'Keeffe, M.; Yaghi, O. M. Colossal Cages in Zeolitic Imidazolate Frameworks as Selective Carbon Dioxide Reservoirs. *Nature* **2008**, *453*, 207-211.

(17) Liu, S.; Xiang, Z.; Hu, Z.; Zheng, X.; Cao, D. Zeolitic Imidazolate Framework-8 as a Luminescent Material for the Sensing of Metal Ions and Small Molecules. *J. Mater. Chem.* **2011**, *21*, 6649-6653.

(18) Peralta, D.; Chaplais, G.; Simon-Masseron, A.; Barthelet, K.; Chizallet, C.; Quoineaud, A.-A.; Pirngruber, G. D. Comparison of the Behavior of Metal–Organic Frameworks and Zeolites for Hydrocarbon Separations. *J. Am. Chem. Soc.* **2012**, *134*, 8115-8126.

(19) Lewis, D. W.; Ruiz-Salvador, A. R.; Gómez, A.; Rodriguez-Albelo, L. M.; Coudert, F.-X.; Slater, B.; Cheetham, A. K.; Mellot-Draznieks, C. Zeolitic Imidazole Frameworks: Structural and Energetics Trends Compared with Their Zeolite Analogues. *Crystengcomm* **2009**, *11*, 2272-2276.

(20) Karagiaridi, O.; Bury, W.; Sarjeant, A. A.; Stern, C. L.; Farha, O. K.; Hupp, J. T. Synthesis and Characterization of Isostructural Cadmium Zeolitic Imidazolate Frameworks via Solvent-assisted Linker Exchange. *Chem. Sci.* **2012**, *3*, 3256-3260.

(21) Shahzad, F.; Alhabeb, M.; Hatter, C. B.; Anasori, B.; Man Hong, S.; Koo, C. M.; Gogotsi, Y. Electromagnetic Interference Shielding with 2D Transition Metal Carbides (MXenes). *Science* **2016**, *353*, 1137-1140.

(22) Feng, W.; Wang, Y.; Chen, J.; Li, B.; Guo, L.; Ouyang, J.; Jia, D.; Zhou, Y. Metal Organic Framework-Derived CoZn Alloy/N-doped Porous Carbon Nanocomposites: Tunable Surface Area and Electromagnetic Wave Absorption Properties. *J. Mater. Chem. C* **2018**, *6*, 10-18.

(23) Ma, J.; Zhang, X.; Liu, W.; Ji, G. Direct Synthesis of MOF-Derived Nanoporous CuO/Carbon Composites for High Impedance Matching and Advanced Microwave Absorption. *J. Mater. Chem. C* **2016**, *4*, 11419-11426.

(24) Yin, Y.; Liu, X.; Wei, X.; Li, Y.; Nie, X.; Yu, R.; Shui, J. Magnetically Aligned Co-C/MWCNTs Composite Derived from MWCNT-Interconnected Zeolitic Imidazolate Frameworks for a Lightweight and Highly Efficient Electromagnetic Wave Absorber. *ACS Appl. Mater. Interfaces* **2017**, *9*, 30850-30861.

(25) Yin, Y.; Liu, X.; Wei, X.; Yu, R.; Shui, J., Porous CNTs/Co Composite Derived from Zeolitic Imidazolate Framework: A Lightweight, Ultrathin, and Highly Efficient Electromagnetic Wave Absorber. *ACS Appl. Mater. Interfaces* **2016**, *8*, 34686-34698.

(26) Lv, H.; Yang, Z.; Wang, P. L.; Ji, G.; Song, J.; Zheng, L.; Zeng, H.; Xu, Z. J. A Voltage-Boosting Strategy Enabling a Low-Frequency, Flexible Electromagnetic Wave Absorption Device. *Adv. Mater.* **2018**, *30*, 1706343-1706351.

(27) Lu, S.; Meng, Y.; Wang, H.; Wang, F.; Yuan, J.; Chen, H.; Dai, Y.; Chen, J., Great Enhancement of Electromagnetic Wave Absorption of MWCNTs@Carbonaceous CoO Composites Derived from MWCNTs-Interconnected Zeolitic Imidazole Framework. *Appl. Surf. Sci.* **2019**, *481*, 99-107.

(28) Wang, K.; Chen, Y.; Tian, R.; Li, H.; Zhou, Y.; Duan, H.; Liu, H. Porous Co-C Core-Shell Nanocomposites Derived from Co-MOF-74 with Enhanced Electromagnetic Wave Absorption Performance. *ACS Appl. Mater. Interfaces* **2018**, *10*, 11333-11342.

(29) Lv, H.; Yang, Z.; Ong, S. J. H.; Wei, C.; Liao, H.; Xi, S.; Du, Y.; Ji, G.; Xu, Z. J. A Flexible Microwave Shield with Tunable Frequency-Transmission and Electromagnetic Compatibility. *Adv. Funct. Mater.* **2019**, *29*, 1900163..

(30) Luo, C. J.; Tang, Y. S.; Jiao, T.; Kong, J. High-Temperature Stable and Metal-Free Electromagnetic Wave-Absorbing SiBCN Ceramics Derived from Carbon-Rich Hyperbranched Polyborosilazanes. *ACS Appl. Mater. Interfaces* **2018**, *10*, 28051-28061.

(31) Yin, X.; Kong, L.; Zhang, L.; Cheng, L.; Travitzky, N.; Greil, P. Electromagnetic Properties of Si–C–N Based Ceramics and Composites. *Int. Mater. Rev.* **2014**, *59*, 326-355.

(32) Dai, X.; Du, Y.; Yang, J.; Wang, D.; Gu, J.; Li, Y.; Wang, S.; Xu, B. B.; Kong, J. Recoverable and Self-healing Electromagnetic Wave Absorbing Nanocomposites. *Compos. Sci. Technol.* **2019**, *174*, 27-32.

(33) Luo, C.; Jiao, T.; Gu, J.; Tang, Y.; Kong, J. Graphene Shield by SiBCN Ceramic: A Promising High-Temperature Electromagnetic Wave-Absorbing Material with Oxidation Resistance. *ACS Appl. Mater. Interfaces* **2018**, *10*, 39307-39318.

(34) Luo, C. J.; Jiao, T.; Tang, Y. S.; Kong, J. Excellent Electromagnetic Wave Absorption of Iron-Containing SiBCN Ceramics at 1158K High-Temperature. *Adv. Eng. Mater.* **2018**, *20*, 1-10.

(35) Song, Y.; He, L.; Zhang, X.; Liu, F.; Tian, N.; Tang, Y.; Kong, J. Highly Efficient Electromagnetic Wave Absorbing Metal-Free and Carbon-Rich Ceramics Derived from Hyperbranched Polycarbosilazanes. *J. Phys. Chem. C* **2017**, *121*, 24774-24785.

(36) West, R.; David, L. D.; Djurovich, P. I.; Stearley, K. L.; Srinivasan, K. S. V.; Yu, H. Phenylmethylpolysilanes-Formable Silane Copolymers with Potential Semiconducting Properties. *J. Am. Chem. Soc.* **1981**, *103*, 7352-7354.

(37) Kong, J.; Schmalz, T.; Motz, G.; Müller, A. H. E. Magnetoceramic Nanocrystals from the Bulk Pyrolysis of Novel Hyperbranched Polyferrocenyl(boro)carbosilanes. *J. Mater. Chem. C* **2013**,*1*, 1507-1514.

(38) Corriu, R. J. P.; Guerin, C.; Henner, B.; Kuhlmann, T.; Jean, A.; Garnier, F.; Yassar, A. Organosilicon Polymers-Synthesis of Poly[(silanylene)diethynylene]swith Conducting Properties. *Chem. Mater.* **1990**, *2*, 351-352.

(39) Luo, C. J.; Duan, W. Y.; Yin, X. W.; Kong, J. Microwave-Absorbing Polymer-Derived Ceramics from Cobalt-Coordinated Poly(dimethylsilyiene)diacetylenes. *J. Phys. Chem. C* **2016**, *120*, 18721-18732.

(40) Wu, R.; Xue, Y.; Liu, B.; Zhou, K.; Wei, J.; Chan, S. H. Cobalt Diselenide Nanoparticles Embedded within Porous Carbon Polyhedra as Advanced Electrocatalyst for Oxygen Reduction Reaction. *J. Power Sources* **2016**, *330*, 132-139.

(41) Torad, N. L.; Hu, M.; Ishihara, S.; Sukegawa, H.; Belik, A. A.; Imura, M.; Ariga, K.; Sakka, Y.; Yamauchi, Y. Direct Synthesis of MOF-Derived Nanoporous Carbon with Magnetic Co Nanoparticles toward Efficient Water Treatment. *Small* **2014**, *10*, 2096-2107.

(42) Jiang, Z.; Li, Z. P.; Qin, Z. H.; Sun, H. Y.; Jiao, X. L.; Chen, D. R. LDH Nanocages Synthesized with MOF Templates and Their High Performance as Supercapacitors. *Nanoscale* **2013**, *5*, 11770-11775.

(43) Lerf, A.; He, H.; Forster, M.; Klinowski, J. Structure of Graphite Oxide Revisited. *J. Phys. Chem. B* **1998**, 102, 4477−4482.

(44) Miles, P. A.; Westphal, W. B.; Von Hippel, A. Dielectric Spectroscopy of Ferromagnetic Semiconductors. *Rev. Mod. Phys.* 1**957**, 29, 279−307.

(45) You, B.; Jiang, N.; Sheng, M.; Drisdell, W. S.; Yano, J.; Sun, Y. Bimetal–Organic Framework Self-Adjusted Synthesis of Support-Free Nonprecious Electrocatalysts for Efficient Oxygen Reduction. *ACS Catal.* **2015**, *5*, 7068-7076.

(46) Wu, R.; Wang, D. P.; Rui, X.; Liu, B.; Zhou, K.; Law, A. W.; Yan, Q.; Wei, J.; Chen, Z. In-situ Formation of Hollow Hybrids Composed of Cobalt Sulfides Embedded within Porous Carbon Polyhedra/carbon Nanotubes for High-performance Lithium-ion Batteries. *Adv. Mater.* **2015**, *27*, 3038-3044.

(47) Tang, J.; Salunkhe, R. R.; Liu, J.; Torad, N. L.; Imura, M.; Furukawa, S.; Yamauchi, Y. Thermal Conversion of Core–Shell Metal–Organic Frameworks: A New Method for Selectively Functionalized Nanoporous Hybrid Carbon. *J. Am. Chem. Soc.* **2015**, *137*, 1572-1580.

(48) Xia, W.; Zhu, J.; Guo, W.; An, L.; Xia, D.; Zou, R. Well-defined Carbon Polyhedrons Prepared from Nano Metal–organic Frameworks for Oxygen Reduction. *J. Mater. Chem. A* **2014**, *2*, 11606-11613.

(49) Bhat, I.; Husain, S.; Khan, W.; Patil, S. I. Effect of Zn Doping on Structural, Magnetic and Dielectric Properties of $LaFeO_3$Synthesized through Sol-gel Auto-combustion Process. *Mater. Res. Bull.* **2013**, *48*, 4506-4512.

(50) Jacobs, B. W.; Houk, R. J. T.; Anstey, M. R.; House, S. D.; Robertson, I. M.; Talin, A. A.; Allendorf, M. D. Ordered Metal Nanostructure Self-assembly using Metal–organic Frameworks as Templates. *Chem. Sci.* **2011**, *2*, 411-416.

(51) Lu, S.; Meng, Y.; Wang, H.; Wang, F.; Yuan, J.; Chen, H.; Dai, Y.; Chen, J., Great Enhancement of Electromagnetic Wave Absorption of Mwcnts@Carbonaceous CoO Composites Derived from Mwcnts-Interconnected Zeolitic Imidazole Framework. *Appl. Surf. Sci.* **2019**, 481, 99-107.

(52) Fang, J.; Liu, T.; Chen, Z.; Wang, Y.; Wei, W.; Yue, X.; Jiang, Z., A Wormhole-Like Porous Carbon/Magnetic Particles Composite as an Efficient Broadband Electromagnetic Wave Absorber. *Nanoscale* **2016**, 8, 8899-8909.

(53) Chen, Y. Z.; Wang, C.; Wu, Z. Y.; Xiong, Y.; Xu, Q.; Yu, S. H.; Jiang, H. L. From Bimetallic Metal-Organic Framework to Porous Carbon: High Surface Area and Multicomponent Active Dopants for Excellent Electrocatalysis. *Adv. Mater.* **2015**, *27*, 5010-6.

(54) Salunkhe, R. R.; Tang, J.; Kamachi, Y.; Nakato, T.; Kim, J. H.; Yamauchi, Y. Asymmetric Supercapacitors Using 3D Nanoporous Carbon and Cobalt Oxide Electrodes Synthesized from a Single Metal–Organic Framework. *ACS Nano* **2015**, *9*, 6288-6296.

(55) Zhao, W.; Kong, J.; Liu, H.; Zhuang, Q.; Gu, J.; Guo, Z. Ultra-high Thermally Conductive and Rapid Heat Responsive Poly(benzobisoxazole) Nanocomposites with Self-Aligned Graphene. *Nanoscale* **2016**, *8*, 19984-19993.

(56) Bhadra, B. N.; Song, J. Y.; Khan, N. A.; Jhung, S. H. TiO_2-Containing Carbon Derived from a Metal-Organic Framework Composite: A Highly Active Catalyst for Oxidative Desulfurization. *ACS Appl. Mater. Interfaces* **2017**, *9*, 31192-31202.

(57) Zhao, W. F.; Tang, Y. S.; Xi, J.; Kong, J. Functionalized Graphene Sheets with Poly(ionic liquid)s and High Adsorption Capacity of Anionic Dyes. *Appl. Surf. Sci.* **2015**, *326*, 276-284.

(58) Chen, H.; Wang, M. Q.; Yu, Y.; Liu, H.; Lu, S. Y.; Bao, S. J.; Xu, M. Assembling Hollow Cobalt Sulfide Nanocages Array on Graphene-like Manganese Dioxide Nanosheets for Superior Electrochemical Capacitors. *ACS Appl. Mater. Interfaces* **2017**, *9*, 35040-35047.

(59) Song, Z.; Liu, W.; Cheng, N.; Norouzi Banis, M.; Li, X.; Sun, Q.; Xiao, B.; Liu, Y.; Lushington, A.; Li, R.; Liu, L.; Sun, X. Origin of the High Oxygen Reduction Reaction of Nitrogen and Sulfur co-doped MOF-derived Nanocarbon Electrocatalysts. *Mater. Horiz.* **2017**, *4*, 900-907.

(60) Wang, B.; Wang, Y.; Lei, Y.; Wu, N.; Gou, Y.; Han, C. Tailoring of Porous Structure in Macro-Meso-Microporous SiC Ultrathin FibersviaElectrospinning Combined with Polymer-Derived Ceramics Route. *Mater. Manuf. Process* **2015**, *31*, 1357-1365.

(61) Ashiq, M. N.; Qureshi, R. B.; Malana, M. A.; Ehsan, M. F. Fabrication, Structural, Dielectric and Magnetic Properties of Tantalum and Potassium Doped M-type Strontium Calcium Hexaferrites. *J. Alloy. Compd.* **2015**, *651*, 266-272.

(62) Xia, W.; Zou, R.; An, L.; Xia, D.; Guo, S. A Metal–organic Framework Route to in situ Encapsulation of Co@Co_3O_4@C Core@Bishell Nanoparticles into a Highly Ordered Porous Carbon Matrix for Oxygen Reduction. *Energy Environ. Sci.* **2015**, *8*, 568-576.

(63) Li, G.; Wang, L.; Li, W.; Ding, R.; Xu, Y. $CoFe_2O_4$ and/or Co_3Fe_7Loaded Porous Activated Carbon Balls as a Lightweight Microwave Absorbent. *Phys. Chem. Chem. Phys.* **2014**, *16*, 12385-12392.

(64) Wang, L. X.; Guan, Y. K.; Qiu, X.; Zhu, H. L.; Pan, S. B.; Yu, M. X.; Zhang, Q. T. Efficient Ferrite/Co/Porous Carbon Microwave Absorbing Material based on Ferrite@Metal-Organic Framework. *Chem. Eng. J.* **2017**, *326*, 945-955.

(65) Quan, B.; Liang, X. H.; Ji, G. B.; Ma, J. N.; Ouyang, P. Y.; Gong, H.; Xu, G. Y.; Du, Y. M. Strong Electromagnetic Wave Response Derived from the Construction of Dielectric/Magnetic Media Heterostructure and Multiple Interfaces. *ACS Appl. Mater. Interfaces* **2017**, *9*, 9964-9974.

(66) Zhang, K.; Wu, F.; Xie, A. M.; Sun, M. X.; Dong, W. In Situ Stringing of Metal Organic Frameworks by SiC Nanowires for High-Performance Electromagnetic Radiation Elimination. *ACS Appl. Mater. Interfaces* **2017**, *9*, 33041-33048.

(67) Zhao H. Q.; Cheng, Y.; Ma, J. N.; Zhang, Y. N.; Ji, G. B. A Sustainable Route from Biomass Cotton to Construct Lightweight and High-Performance Microwave Absorber. *Chem. Eng. J.***2018**, *339*. 432-441.

(68) Ohkoshi, S.-I.; Kuroki, S.; Sakurai, S.; Matsumoto, K.; Sato, K.; Sasaki, S., A Millimeter-Wave Absorber Based on Gallium-Substituted ε-Iron Oxide Nanomagnets. *Angew. Chem. Int. Ed.* **2007**, *46*, 8392-8395.

(69) Cao, M.-S.; Yang, J.; Song, W.-L.; Zhang, D.-Q.; Wen, B.; Jin, H.-B.; Hou, Z.-L.; Yuan, J. Ferroferric Oxide/Multiwalled Carbon Nanotube vs Polyaniline/Ferroferric Oxide/Multiwalled Carbon Nanotube Multiheterostructures for Highly Effective Microwave Absorption. *ACS Appl. Mater. Interfaces* **2012**, *4*, 6948-6955.

(70) Fang, J.; Liu, T.; Chen, Z.; Wang, Y.; Wei, W.; Yue, X.; Jiang, Z., A Wormhole-Like Porous Carbon/Magnetic Particles Composite as an Efficient Broadband Electromagnetic Wave Absorber. *Nanoscale* **2016**, *8*, 8899-8909.

The Table of Contents Entry